Element-specific magnetization redistribution at $YBa_2Cu_3O_7/La_{2/3}Ca_{1/3}MnO_3$ interfaces

A. Alberca,[1,2,*] M. A. Uribe-Laverde,[2] Y. W. Windsor,[1] M. Ramakrishnan,[1] L. Rettig,[1]
I. Marozau,[2] J-M. Tonnerre,[3,4] J. Stahn,[5] U. Staub,[1] and C. Bernhard[2]
[1]*Swiss Light Source, Paul Scherrer Institut, CH-5232 Villigen PSI, Switzerland*
[2]*University of Fribourg, Department of Physics and Fribourg Centre for Nanomaterials, Chemin du Musee 3, CH-1700 Fribourg, Switzerland*
[3]*Université Grenoble Alpes, Institut NEEL, F-38042 Grenoble, France*
[4]*CNRS, Institut NEEL, F-38042 Grenoble, France*
[5]*Laboratory for Neutron Scattering, Paul Scherrer Institut, CH-5232 Villigen PSI, Switzerland*
(Received 17 September 2015; revised manuscript received 20 October 2015; published 17 November 2015)

We study the element-specific magnetic depth profiles of a $YBa_2Cu_3O_7/La_{2/3}Ca_{1/3}MnO_3$ (YBCO/LCMO) superlattice using soft x-ray resonant magnetic reflectometry (XRMR). This allows us to study the magnetic proximity effect (MPE) that is observed at the YBCO/LCMO interface, characterized by the occurrence of a depleted layer on the manganite side and an induced magnetization in the YBCO. Using the element-specific depth profiling capability of XRMR, we show that the Cu moments ($0.28\mu_B$ per interfacial Cu ion) reside on the YBCO side of the interface and originate from the CuO_2 plane that is located at the interface. We also rule out the possibility that the Cu moments originate from the migration of Cu atoms into the LCMO layer (interdiffusion). Finally, we show that the suppression of the Mn moment on the LCMO side is only partial for the interface of LCMO deposited on YBCO ($0.62\mu_B$ per Mn ion), compared to the complete suppression for the interface of YBCO deposited on LCMO. These differences in the LCMO depleted layers indicate the strong variations in the MPE between the case of YBCO on LCMO and the case of LCMO on YBCO.

DOI: 10.1103/PhysRevB.92.174415 PACS number(s): 75.70.Cn, 75.25.−j, 74.78.Fk, 61.05.cm

I. INTRODUCTION

The properties of interfaces in heterostructures made of complex oxides with strongly correlated electrons are the subject of intense research [1,2]. The strongly correlated d electrons in bulk transition metal oxides play a crucial role for magnetic properties, thermal transport, and electric conductivity, giving rise to a variety of interesting effects, such as metal-insulator transitions, multiferroicity, and superconductivity [3]. These effects are closely related to the intimate coupling between the magnetic, orbital, and lattice degrees of freedom.

In heterostructures, nearly competing (i.e., almost degenerate) ground states also give rise to novel effects at the interface. Prominent examples are the two-dimensional electron gas exhibited by $LaAlO_3/SrTiO_3$ heterostructures [4] or the interfacial control of the orbital polarization in $LaNiO_3/LaAlO_3$ superlattices [5,6]. These properties can be controlled by external stimuli, such as electric or magnetic fields and strain.

Another example is the coupling between the antagonistic superconducting (SC) and ferromagnetic (FM) orders. In particular, in superlattices consisting of the optimally doped ferromagnetic manganite $La_{2/3}Ca_{1/3}MnO_3$ (LCMO) and the high-T_c superconductor $YBa_2Cu_3O_7$ (YBCO), a magnetic proximity effect (MPE) occurs, characterized by (i) a suppression of the FM order of the LCMO's Mn moments close to the interface (depleted layers) and (ii) induced Cu net magnetization in YBCO that aligns antiparallel to the magnetization of the Mn [7–10].

The LCMO depleted layers were first reported using polarized neutron reflectometry (PNR) [7]. PNR exploits the neutrons' sensitivity to the nuclear and magnetic potentials, which allow exploring structural and magnetic properties of layered heterostructures. Full reconstruction of the reflectivity data cannot be performed due to the loss of phase information, but structural and magnetic profiles can be obtained by fitting the data to mathematical models [11]. It has been suggested that the LCMO depleted layers retain a nonzero magnetization [10]. The existence of induced Cu moments was firmly established by x-ray magnetic circular dichroism (XMCD) measurements in Ref. [9], where the two aforementioned manifestations of the MPE where reported to occur simultaneously. Further characterization of this system revealed a suppression of the SC transition temperature, accompanied by a reduction of Curie temperature of the manganite [12,13]. Finally, scanning transmission electron microscopy experiments showed that the CuO chains of the YBCO are missing at the interface such that the CuO_2 planes have a straight bond via the apical oxygen to the MnO_2 planes at the other side of the interface [14].

The two manifestations of the MPE in YBCO/LCMO heterostructures have been interpreted in terms of a transfer of electrons from LCMO to YBCO across the interface (of about 0.2 electrons per Cu atom [15]) and an orbital reconstruction of the Cu e_g levels. The latter is most likely related to hybridization between the Cu and Mn $d_{3z^2-r^2}$ orbitals via the apical oxygen ion, which leads to a partial occupation of the Cu $d_{3z^2-r^2}$ orbitals (in contrast to the fully occupied state in bulk YBCO). This reduces the overall orbital anisotropy, as revealed by x-ray linear dichroism (XLD) at the Cu L_3 edge [15], and may cause a strong antiferromagnetic exchange coupling between Cu and Mn. Recent studies on $La_{2-x}Sr_xCuO_4$/LCMO heterostructures have demonstrated that these electronic and magnetic proximity effects are coupled and are common to these cuprate/manganite heterostructures [16].

XMCD and PNR are complementary techniques, but they either lack spatial resolution (in the case of XMCD) or

*aurora.alberca@psi.ch

sensitivity to weak magnetic signals and element specificity (in the case of PNR). Due to these limitations, some questions remain open. For instance, the precise location of the ferromagnetic Cu moments is unknown, as is the nature of magnetization in the LCMO depleted layers. To clarify these points, we use x-ray resonant magnetic reflectometry (XRMR). XRMR is a powerful technique that can probe electronic and magnetic states at interfaces with a high depth resolution and that combines: (1) element specificity (due to use of photon energies which are tuned to resonances), (2) sensitivity to the orientation of the magnetic moments via the polarization of the x rays and, (3) high spacial resolution (to the subnanometer level) as a consequence of the interference between x-rays reflected at each interface in the heterostructure. XRMR has been previously used in LCMO/YBCO bilayers to study the LCMO magnetic profile [17]. That study found that the magnetization of LCMO is modified not only near the interface with the superconductor, but also at the interface with the $SrTiO_3$ substrate. In an additional study simulations of the XRMR data suggested that the Cu magnetic moments are located in the YBCO layer and do not originate from Cu ions that may have diffused into the LCMO layers [9].

Here, we present a detailed XRMR study which provides a wealth of additional information about the MPE on the YBCO and the LCMO sides of the interface of YBCO/LCMO superlattices (SLs). We determine the structural and magnetic depth profiles for YBCO/LCMO SLs from reflectivity measurements using photon energies near the L_3 absorption edges of the Cu and Mn atoms. We demonstrate that the Cu moments reside on the YBCO side and we show that they originate from a single CuO_2 plane located at the interface. The case of an interdiffusion of Cu ions into the LCMO is broadly considered and is clearly excluded. We also show that the suppression of the Mn moment on the LCMO side is incomplete, confirming that the MPE at the interface in which LCMO is grown on YBCO is different to the one in which YBCO is grown on LCMO.

In Sec. II details of the LCMO/YBCO SL structure and macroscopic characterization are given, the experimental method to measure XRMR is described, and the analysis process is considered. In Sec. III results and discussion are presented. This section is divided into three subsections: Sec. III A, in which the process to obtain the scattering amplitudes is described; Sec. III B, in which the structure of the YBCO/LCMO SL is characterized, and Sec. III C, in which Mn and Cu absorption edges and magnetic depth profiles are considered separately. The case of the Mn absorption edge is presented using three different models and the sensitivity of XRMR to the fine details of the Mn magnetic profiles studied for different configurations of the thickness and magnetization of the LCMO depleted layers. The case of the Cu absorption edge is thoroughly studied in the last subsection, where the case of interdiffusion is considered.

II. EXPERIMENTAL

A $[YBa_2Cu_3O_7/La_{2/3}Ca_{1/3}MnO_3]_{10}$ superlattice (YBCO/LCMO SL) was grown with pulsed laser deposition (PLD) on a $La_{0.3}Sr_{0.7}Al_{0.65}Ta_{0.35}O_3$ (001) (LSAT) substrate which has already been characterized and studied in Refs. [14] and [10]. Each layer has a nominal thickness of 100 Å. The onset

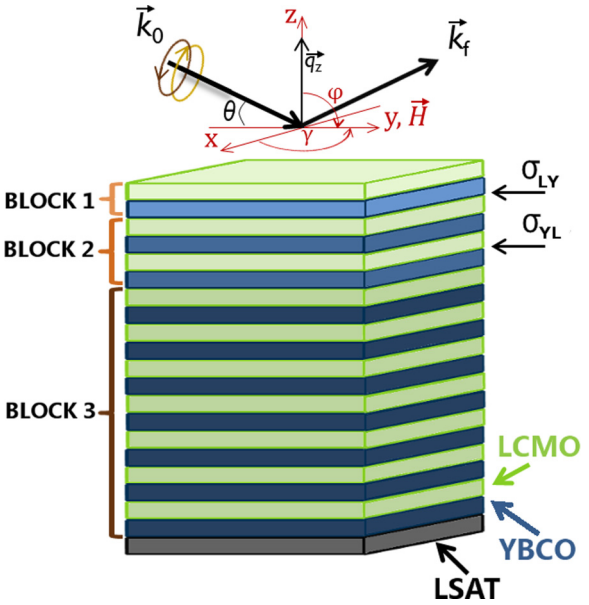

FIG. 1. (Color online) Sketch of the YBCO/LCMO superlattice. YBCO (LCMO) layers are shown in blue (green). σ_{YL} and σ_{LY} are the roughness of the YBCO/LCMO and LCMO/YBCO interfaces, respectively, according to the growth direction. The diagram shows the geometry of the XRMR experiment, where $\vec{k}_0$ is the wave vector of the circularly polarized incident beam and $\vec{k}_f$ the wave vector of the reflected beam, and $\vec{q}_z$ the momentum transfer. θ is the incidence angle and $\vec{H}$ indicates the direction of the applied magnetic field.

of its superconducting transition is observed in resistivity curves at $T_C \approx 88$ K. Magnetization was measured after field cooling with a 4 kOe field applied in plane. The ferromagnetic transition was found at $T_{Curie} \approx 200$ K. At 10 K the saturation magnetization reaches an average value of 2.1 μ_B per Mn ion, which is smaller than the bulk LCMO value of 3.7 μ_B per Mn ion.

The x-ray resonant reflectometry (XRR) and x-ray resonant magnetic reflectometry (XRMR) measurements were performed with the RESOXS [18] end station at the X11MA beamline of the Swiss Light Source [19]. The sample was mounted on a cold finger and a magnetic field was applied in the film plane using a permanent magnet which provides a field of about 0.2 T at the sample surface. The sample was field-cooled to saturate the FM layers (coercive field <0.04 T at 10 K). All low-T measurements were performed in the remanent state of the sample. The reflected intensity I was collected in the $\theta/2\theta$ two-circle geometry (see Fig. 1), where θ is the incident angle on the sample surface. At each angle the handedness of helicity of the circularly polarized x rays was flipped.

The structure of the SL was characterized with room-temperature and low-temperature reflectivity curves (XRR), as follows. Room-temperature (250 K) curves were measured with unpolarized light at the Cu and Mn L_3 edges, and low-temperature curves (10 K) were collected using nonresonant photon energies and unpolarized light. Subsequently, the same structural parameters were used for fitting models to the XRMR curves at low temperatures. XRMR measurements at 10 K (well below the Curie temperature of LCMO) were carried out in remanence, with the LCMO magnetization

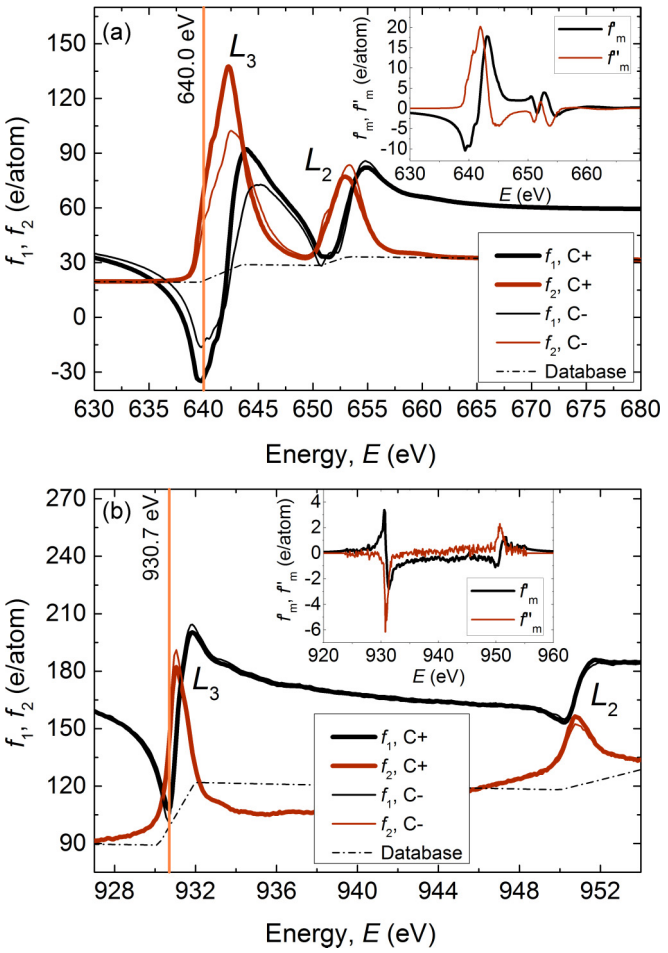

FIG. 2. (Color online) Atomic scattering amplitudes for LCMO (a) and YBCO (b) as functions of energy (containing the magnetic contribution at 10 K) with an applied field of 0.5 T. $f_1(E)$ and $f_2(E)$ are the real and imaginary part of the scattering amplitudes, respectively. f''_m is the extracted magnetic contribution. The dashed line shows the imaginary part of the scattering amplitudes obtained from the database [28]. The indicated energies $E_{Mn} = 640.0$ eV and $E_{Cu} = 930.7$ eV were used for the XRMR measurements. Insets: Pure magnetic contributions to the scattering amplitudes around the Cu and Mn $L_{3,2}$ edges.

aligned either parallel or antiparallel to the y direction (see Fig. 1) and using circularly polarized light. The asymmetry ratio is calculated as $A = (I_{C+} - I_{C-})/(I_{C+} + I_{C-})$. θ varied in the range of 0°–29.8° and 0°–22.0°, for E_{Mn} and E_{Cu}, respectively, to avoid the interference with signals from the [001] broad Bragg peak of YBCO.

The scattering amplitudes f were extracted from x-ray absorption spectra (XAS) data collected in total electron yield mode (Fig. 2) at the X07MA beamline of the Swiss Light Source [20] with equivalent energy resolution and conditions. For the XAS spectra, a saturating magnetic field of 0.5 T was applied along the in-plane projection of the beam direction. Element-specific magnetization curves were measured at the UE56/2-PGM1 beamline [21] of the BESSY II light source at the Helmholtz-Zentrum Berlin (HZB) to determine the magnitude of the magnetization in remanence. The photon energies to measure the XRR and XRMR reflectivity curves were chosen from the XAS spectra to be $E_{Mn} = 640.0$ eV and $E_{Cu} = 930.7$ eV.

For analyzing the measured reflectivity curves we used the software DYNA [22], which is written in MATLAB code and allows fitting the room-temperature reflectivity curves using Parratt's formalism [23] and the magnetic reflectivity curves using the 4-Matrix formalism described by Elzo *et al.* [22]. The reflectivity models were derived following a classical approach in which the medium is characterized using the Maxwell equations and the dielectric susceptibility tensor (calculated from the scattering amplitudes). This method is based on the formalism of Ref. [24]. Off-diagonal terms of the dielectric susceptibility tensor with order higher than 1 are neglected (e.g., components that depend quadratically on the magnetic moment); this ensures that the eigenwaves propagating in the magnetic medium are circularly polarized waves [22]. The goodness of the fit (GOF) is calculated using $l_{red} = (1/\nu)\sum_i (I_i^{meas} - I_i^{calc})^2/s^2$, where I^{meas} and I^{calc} are the measured and calculated intensities, respectively, s is the standard deviation, and ν the number of degrees of freedom. In the case of the room-temperature reflectometry, reflectivity curves were normalized. We estimated the errors from the confidence interval in which the GOF does not change substantially when varying each parameter individually.

III. X-RAY RESONANT MAGNETIC REFLECTOMETRY

A. Absorption spectra

1. Atomic scattering factors

Analysis of XRMR data requires determining the optical constants of the individual layers of the heterostructure in the x-ray regime (energy-dependent complex index of refraction). Resonant and magnetic contributions are calculated from the quantum-mechanical treatment of the atomic scattering process [25] and through the optical theorem. Following Elzo *et al.* [22] and Stepanov and Sinha [24], in the case of a magnetic resonance, the total amplitude for coherent elastic scattering of x rays from a magnetically homogeneous medium can be expressed in terms of the incident and scattered photon polarization states [26]:

$$f = f_0 + \frac{3\lambda}{8\pi}[F_{11} + F_{1\bar{1}}](\mathbf{e}_\mathbf{f}^* \cdot \mathbf{e}_\mathbf{i}^*) - \frac{3\lambda}{8\pi} i[F_{11} - F_{1\bar{1}}](\mathbf{e}_\mathbf{f}^* \times \mathbf{e}_\mathbf{i}^*) \cdot \mathbf{M}, \quad (1)$$

where $\mathbf{e}_\mathbf{i}^*$ and $\mathbf{e}_\mathbf{f}^*$ are the electric polarization vectors of the incident and reflected light and $\mathbf{M}$ is the magnetization. The first two terms of Eq. (1) correspond to the nonresonant and the resonant nonmagnetic (charge) contributions to the (energy-dependent) scattering amplitudes. $f_0 = r_0[-Z + f'(E) + i f''(E)]$ is the charge scattering amplitude, in which r_0 is the classical electron radius, and Z is the number of electrons in the atom. f_0 contains the Thomson scattering and the dispersion corrections, $f'(E) + i f''(E)$, with E being the x-ray photon energy. The third term of Eq. (1) represents the magnetic contribution. The F_{1m} functions are the resonant magnetic scattering factors and are proportional to the probability of absorption of a photon by an atom with a change of m in its atomic angular momentum [25]. Higher orders of

the multipoles are neglected, since these are not expected to contribute significantly in the soft x-rays regime [27].

2. *Absorption spectra*

The imaginary part of the scattering amplitude $f_2(E)$ can be obtained from an XAS experiment as follows. The collected XAS data contain the nonresonant, resonant, and the magnetic contributions to the scattering amplitudes. We call $f''_{\mathrm{r}}(E)$ [$f'_{\mathrm{r}}(E)$] the imaginary (real) part of the scattering amplitudes that contain the resonant and nonresonant non-magnetic contributions [described in the first two terms in Eq. (1)] and $f''_{\mathrm{m}}(E)$ [$f'_{\mathrm{m}}(E)$] the imaginary (real) part of the magnetic contribution [given by the third term in Eq. (1)]. Then, the imaginary part of the scattering amplitudes can be expressed as $f_2(E) = f''_{\mathrm{r}}(E) + f''_{\mathrm{m}}(E)$ and can be calculated by normalizing the of-resonance region of the XAS (before and after the edge) to the tabulated atomic values of the compound [28]. The real part $f_1(E) = f'_{\mathrm{r}}(E) + f'_{\mathrm{m}}(E)$ is extracted from the imaginary part by the Kramers-Kronig transformation [29]. $f''_{\mathrm{m}}(E)$ can be separated from $f_2(E)$ by measuring the XAS for right- (C+) and left- (C-) handed circular polarizations [22] and calculating the difference of intensities as $(I_{C+} - I_{C-})/2$. Figure 2 presents the real f_1 (calculated) and imaginary f_2 (extracted) parts of the scattering amplitudes around the Cu and Mn $L_{3,2}$ edges. Insets show the pure magnetic contribution f_{m}. Due to the MPE, a magnetic contribution is expected around the Cu $L_{2,3}$ edges. f''_{m} for Cu and Mn exhibit inverted signals around the L_3 edge, indicating the antiparallel alignment of the Mn and Cu moments [see insets in Fig. 2(a)].

B. Structure characterization

XRR was used to characterize the thickness (t), roughness (σ), and density (ρ), and thus to obtain the structural profile of the heterostructure. Reflectivity curves at the energies E_{Mn} and E_{Cu} were measured at 250 K, above the Curie temperature of LCMO. The densities of the materials were kept fixed to the nominal values according to their composition ($\rho_{\mathrm{LCMO}} = 6.08\,\mathrm{g/cm^3}$, $\rho_{\mathrm{YBCO}} = 6.37\,\mathrm{g/cm^3}$) and assumed to be constant across the SL. The validity of this assumption relies in the epitaxial growth of the layers, with no changes in the lattice parameters, and the nearly full oxygenation of the YBCO/LCMO layers [14]. The thicknesses and roughnesses of the layers were fitted to a structural model. To improve the fits, the superlattice was divided into three different blocks (see Fig. 1) consisting of seven, two, and one bilayers (starting from the substrate). Different thicknesses and roughnesses were considered for each of these blocks. Due to the limited penetration depth of soft x rays, the sensitivity to properties of the bilayers closer to the substrate is significantly reduced, even at large incident angles. Additionally, the uppermost LCMO layer was divided into two sublayers and the density of the upper sublayer was fitted as an independent parameter to take into account a partial degradation of the LCMO that results in a reduced density, $\rho = 2.62 \pm 0.01\,\mathrm{g/cm^3}$.

Figure 3 presents the XRR data taken at E_{Mn} and E_{Cu} and the corresponding fits to the model. The resulting average thickness (weighted according the number of layers in each block) is (96 ± 2) Å for the YBCO layers and (94 ± 1) Å for the LCMO layers (see Table I). The roughness is defined as

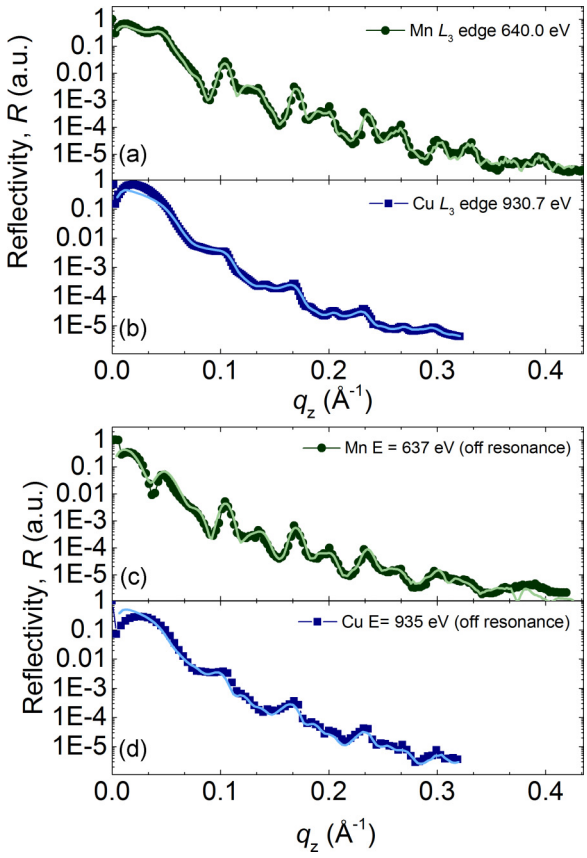

FIG. 3. (Color online) (a, b) Resonant x-ray reflectivity curves without magnetic contrast taken at room temperature. Lines are the corresponding fits. (c, d) Reflectivity curves measured at 10 K using unpolarized light below the Mn L_3 resonance and above the Cu L_3 resonance, respectively.

follows: σ_{YL} is the roughness of the interface for LCMO grown on top of YBCO and σ_{LY} the roughness for YBCO grown on top of LCMO. We obtained a weighted average roughness of $\sigma_{\mathrm{LY}} = (11 \pm 2)$ Å and $\sigma_{\mathrm{YL}} = (6 \pm 1)$ Å. The obtained parameters are summarized in Table I. The differences between σ_{YL} and σ_{LY} are in good agreement with transmission electron microscopy data [14] and most probably are the result of the PLD growing process and the differences between growing LCMO on YBCO, as compared to growing YBCO on LCMO.

TABLE I. Structural parameters of the LCMO/YBCO SL. The thickness (t) and roughness (σ) are given with their error estimates for the LCMO and YBCO layers for each block, as depicted in Fig. 1. The average values, weighted according to the number of layers in each block, are also given. For block 1, two values of the thickness are given for the two LCMO sublayers considered. The total thickness of the uppermost LCMO layer is 96 Å. The goodness of the fit l_{red}, also given, is calculated as described in the text.

		Block 1	Block 2	Block 3	Av.
LCMO	$t(\pm 1$ Å)	86/10	93	94	94
($l_{\mathrm{red}} = 0.034$)	$\sigma_{LY}(\pm 2$ Å)	5	10	13	11
YBCO	$t(\pm 2$ Å)	100	96	96	96
($l_{\mathrm{red}} = 0.069$)	$\sigma_{YL}(\pm 1$ Å)	9	6	5	6

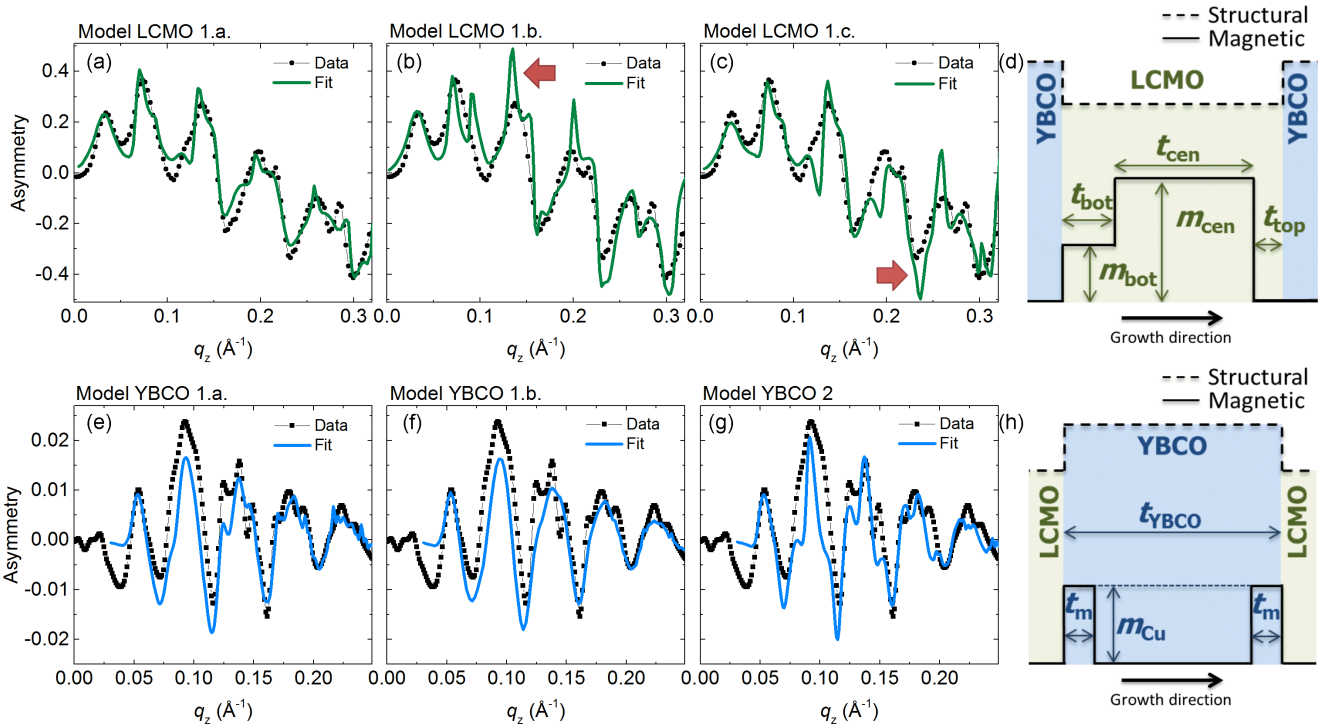

FIG. 4. (Color online) Asymmetry ratio at 10 K for E_{Mn} (panels a, b, and c) and E_{Cu} (panels e, f, and g). (d, h) are sketches of the structural (dashed lines) and magnetic (solid lines) profiles for the Mn and Cu ions, respectively. Red arrows are guides to the eye.

The upper LCMO sublayer, which is partially degraded since it is in contact with the ambient, has a thickness of (10 ± 1) Å. All these values are also in good agreement with previous results using PNR [10] and reveal the high sensitivity of soft x-ray reflectivity to changes in the roughness of the individual layers. This is a result of the different penetration depths at different angles of incidence. Additional reflectivity curves were measured at 10 K off the Mn and Cu L_3 resonances. These curves were modelled using the parameters obtained at high temperatures, confirming that no structural changes occur during cooling [see Figs. 3(c) and 3(d)].

As our results suggest (see Table I), σ_{YL} seems to increase for bilayers closer to the surface. This could be due to the accumulative defects that propagate from one bilayer to another during the growing process. To verify this behavior we fitted the data with a model in which the SL was divided into four distinct blocks. The bottom block consisted of seven bilayers, and the other three blocks were each one bilayer. The layer roughness of each block was taken as a separate parameter. The obtained σ_{YL} values of 4.87, 5.5, 7.4, and 8.5 Å increase from the bottom to the top of the SL and show that the first deposited layers grow with relatively low roughness, and that defects accumulate in subsequently deposited YBCO layers. Nevertheless, σ_{LY} does not change considerably among the four blocks and the GOF only marginally improves when roughness is taken as a free parameter. Therefore, for the remaining of this paper, the three-block model is used to keep to a reasonably low number of fitted parameters.

C. Element-specific magnetic depth profiles

In this section we discuss the magnetic profile of the SL for E_{Mn} and E_{Cu}. We present the fits to different models of the asymmetry [defined as $A = (I_{C+} - I_{C-})/(I_{C+} + I_{C-})$] at each energy. Asymmetries obtained at E_{Mn} and E_{Cu} were fitted separately. In the following, models for the magnetic profile at E_{Mn} and E_{Cu} are denoted as LCMO and YBCO, respectively, and numbered differently. Models with differences in the constrained parameters are distinguished by a letter. For example, model LCMO 1.a and model LCMO 1.b refer to the same magnetic profile and fitting parameters with different constraints between some of these parameters. For all fitted models, the structural parameters, as obtained in Sec. III B, were used. Figures 4(a)–4(c) and 4(e)–4(g) show the asymmetry calculated from the reflectivity curves for E_{Mn} (circles) and E_{Cu} (squares). Figures 4(d) and 4(h) show sketches of the proposed structural and magnetic profiles of the LCMO and YBCO layers, respectively.

Element-specific magnetization curves obtained in reflectivity mode can be used to characterize the magnetic anisotropy [30]. In the case of our YBCO/LCMO SL, the magnetization curves have been used to determine the coupling between the Mn and Cu magnetic moments. Magnetic hysteresis loops were measured at a fixed q_z value, energy, and polarization while sweeping the magnetic field. Figure 5 presents the magnetization curves measured in reflectivity conditions at q_z values that yield a high magnetic contrast while preserving a good signal-to-noise ratio: $q_z = 0.073$ Å^{-1} for E_{Mn} and $q_z = 0.179$ Å^{-1} for E_{Cu}. The magnetization curves in Fig. 5 were scaled using the known saturation magnetization M_{sat} (calculated by applying the XMCD sum rules to the $f''_m(E)$ spectra [9] shown in Fig. 2) and shifted vertically to correct for the structural component of the measured intensity. The E_{Mn} and E_{Cu} magnetization curves exhibit similar magnetic

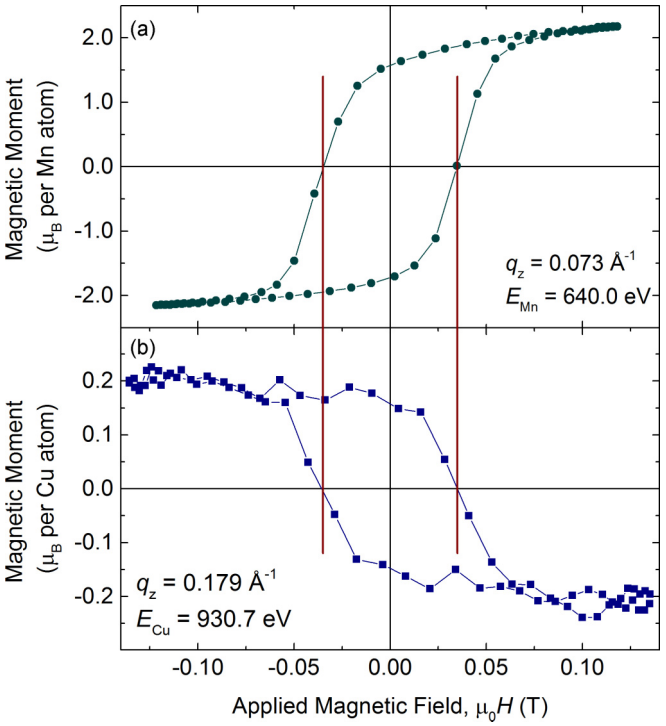

FIG. 5. (Color online) Element-specific Mn (green circles) and Cu (blue squares) magnetization curves measured at 10 K in reflectivity conditions at the indicated q_z values. The magnetization curves are normalized to the saturation values (obtained by applying XMCD sum rules [9] to the f_m'' shown in Fig. 2) and are shifted vertically. The red lines mark the coercive fields for Cu and Mn that are virtually identical, with $H_c = 0.035$ T.

field dependence (similar magnetic anisotropy) and identical coercive fields of $H_c = 0.035$ T.

The magnetic component of the resonant scattering amplitudes f_m (shown in the insets of Fig. 2) were included in the model using Eq. (1). The variations of the magnetization within the heterostructure were considered as follows: f_m was kept fixed throughout the layer but was multiplied by a factor α, which was allowed to vary. The normalized magnetization curves in Fig. 5 were used to calculate the magnetization in remanence $M_{\rm rem}$. The magnetization values [22] across the profile were calculated as $\alpha M_{\rm rem}$. The remanence magnetizations per atom used were $M_{\rm rem}^{\rm Mn} = 1.37\,\mu_B$ and $M_{\rm rem}^{\rm Cu} = 0.17\,\mu_B$.

Finally, the direction of the magnetization was included in the fitted model using two angles, γ and ϕ, which are, respectively, the azimuthal and polar angles (in spherical coordinates) of the magnetization vector (see Fig. 1). At low incident angles, x rays are mostly sensitive to the in-plane component of the magnetization. As the incident angle increases towards normal incidence, x rays can discern magnetic moments canted within the scattering plane [30,31]. This will affect the asymmetry, resulting in almost null asymmetry at high incident angles, when the magnetization is along the y direction ($\gamma = \pm 90^\circ$ and $\phi = 90^\circ$). In addition, the parallel or antiparallel alignment of the magnetization to the y direction ($\gamma = +90^\circ$ or -90°) will result in a reversal between maxima and minima of the asymmetry [22]. This allows unambiguous determination of the direction of the magnetization. In the case of the Mn edge we find $\gamma = 90^\circ$ and $\phi = 90^\circ$, indicating an alignment of the magnetization parallel to the applied magnetic field (y direction). On the other hand, fitting the model to the Cu-edge asymmetry leads only to reasonable agreement for $\gamma = -90^\circ$ and $\phi = 90^\circ$, that is, with a Cu magnetization that is antiparallel to the applied magnetic field.

1. Mn L_3 absorption edge

One of the particularities of the MPE in YBCO/LCMO heterostructure is the suppression of LCMO magnetization near the interface with YBCO, as was previously observed with PNR [7,10]. These layers with a suppressed FM Mn moment were denoted as depleted layers. We find that the asymmetry for LCMO, as shown in Figs. 4(a)–4(c), can only be reasonably described when these depleted layers are taken into account. Models LCMO 1.a, 1.b, and 1.c partition the LCMO layers into three sublayers: bottom, center, and top. The fit parameters are the depleted layer thicknesses $t_{\rm bot}$ and $t_{\rm top}$, and the magnetization of the three sublayers $m_{\rm bot}$, $m_{\rm cen}$, and $m_{\rm top}$. The total thickness of the entire LCMO layer was fixed to the structural parameters, as shown in Sec. III B and in Table I. Models to the LCMO asymmetry were fitted with the same thickness and magnetization parameters of the depleted layers for all blocks (except for the uppermost

TABLE II. Parameters values obtained for the magnetic depth profile of the LCMO layers from the best fits to models LCMO 1.a, LCMO 1.b, and LCMO 1.c. $t_{\rm top}$ and $t_{\rm bot}$ are the thicknesses of the top and bottom depleted layers, respectively. The magnetization values are given for the top and bottom depleted layers and the central part of the LCMO layer. The same thickness and magnetization parameters of the depleted layers are obtained for all blocks (labeled in the table "LCMO"), except for the uppermost LCMO surface sublayer (labeled the "topmost LCMO"). The errors of the magnetization are estimated from the parameter α (see text for more details). The "=" symbol denotes fixed parameters with the same value as the one in the row above. The goodness of the fit $l_{\rm red}$, also given, is calculated as described in the text.

		$t_{\rm top}$ (±1 Å)	$t_{\rm bot}$ (±1 Å)	$m_{\rm top}$ (±0.02 μ_B/Mn)	$m_{\rm cen}$ (±0.02 μ_B/Mn)	$m_{\rm bot}$ (±0.02 μ_B/Mn)
LCMO 1.a	Topmost LCMO	12	22	0.00	1.36	0.62
($l_{\rm red} = 0.047$)	LCMO	11	=	0.01	1.36	=
LCMO 1.b	Topmost LCMO	11	12	0.25	1.29	0.32
($l_{\rm red} = 0.053$)	LCMO	12	=	0.15	1.00	0.44
LCMO 1.c	Topmost LCMO	13	17	0.10	1.08	0.40
($l_{\rm red} = 0.068$)	LCMO	11	19	0.40	1.49	=

LCMO surface sublayer) since no differences in the magnetic profile were found between LCMO layers. Table II lists the best values obtained for the fitted parameters. A sketch of the corresponding profile is shown in Fig. 4(d).

In Ref. [10], analysis of PNR data on the same superlattice was performed with two models, one in which the magnetization of the depleted layers was set to zero and another one in which this magnetization was allowed to vary. The thickness of the LCMO depleted layers was determined with PNR with relatively good accuracy. The obtained values were 9 and 14 Å for the top and bottom depleted layers, respectively. However, the same was not possible for the magnetization. For the second model, a finite magnetic scattering length density was obtained near the bottom interface (with net FM moments of about 20% of the magnetization in the central part of the LCMO layers), but the values for the reduced likelihood estimator (used as the criterion to determine the validity of each model) were similar. As a consequence, it was not possible to conclude whether the FM magnetization in the depleted layers is only partially or fully suppressed. This uncertainty is due to the limited q_z range of the PNR data and to their comparably poor signal-to-noise and signal-to-background ratio.

For the XRMR data, the best fit was obtained with model LCMO 1.a [see Fig. 4(a)]. In this model, the top and bottom depleted layers have different thickness and magnetization values. The top depleted layer has a thickness of (12 ± 1) Å and almost zero magnetization, while the bottom depleted layer has a thickness of (22 ± 1) Å and a nonzero magnetization of nearly 50% of the one in the central sublayer. In model LCMO 1.b we still explore the possibility that the depleted layers are of equal thickness. In this model, we constrain the upper (t_{top}) and lower (t_{bot}) depleted layer thickness to the same value ($t_{\mathrm{top}} = t_{\mathrm{bot}}$) but keep their magnetization separate. The best fit is shown in Fig. 4(b) and the corresponding parameters are listed in Table II. This model fails to reproduce the observed asymmetry; when t_{top} and t_{bot} are constrained to the same value, the magnetization is redistributed to the upper depleted layer, resulting in spikelike features in each oscillation of the asymmetry [marked with a red arrow in Fig. 4(b)]. Model LCMO 1.a indicated that the magnetization of the top depleted layer m_{top} is nearly zero while the bottom depleted layer m_{bot} has a magnetization of $(0.62 \pm 0.02\,\mu_{\mathrm{B}})$ per Mn ion. This result was tested with model LCMO 1.c. There, m_{top} and m_{bot} were constrained to the same value, and t_{top} and t_{bot} remained unconstrained. The best fit is shown in Fig. 4(c) and in Table II. t_{top} and t_{bot} have similar values to those in model LCMO 1.a and the obtained values of $m_{\mathrm{top}} = m_{\mathrm{bot}} = (0.40 \pm 0.02)\mu_B$ per Mn ion are reasonable; the best fit to this model fails to reproduce the observed asymmetry features, particularly at higher q_z values, which exhibit sharper oscillations [see red arrow in Fig. 4(c)]. Notice that the errors of the obtained magnetization are estimated only from those of the parameter α (which originate from the reflectivity data). Our estimation does not include the possible errors associated with the determination of the magnetic contribution to the scattering amplitudes.

Models LCMO 1.a, 1.b, and 1.c. utilize the full extent of the high sensitivity of XRMR to the thickness and the magnetization of the probed layers. To better visualize this, the reflectivity curves of a sample with ten repetitions of identical YBCO/LCMO bilayers with zero roughness were simulated.

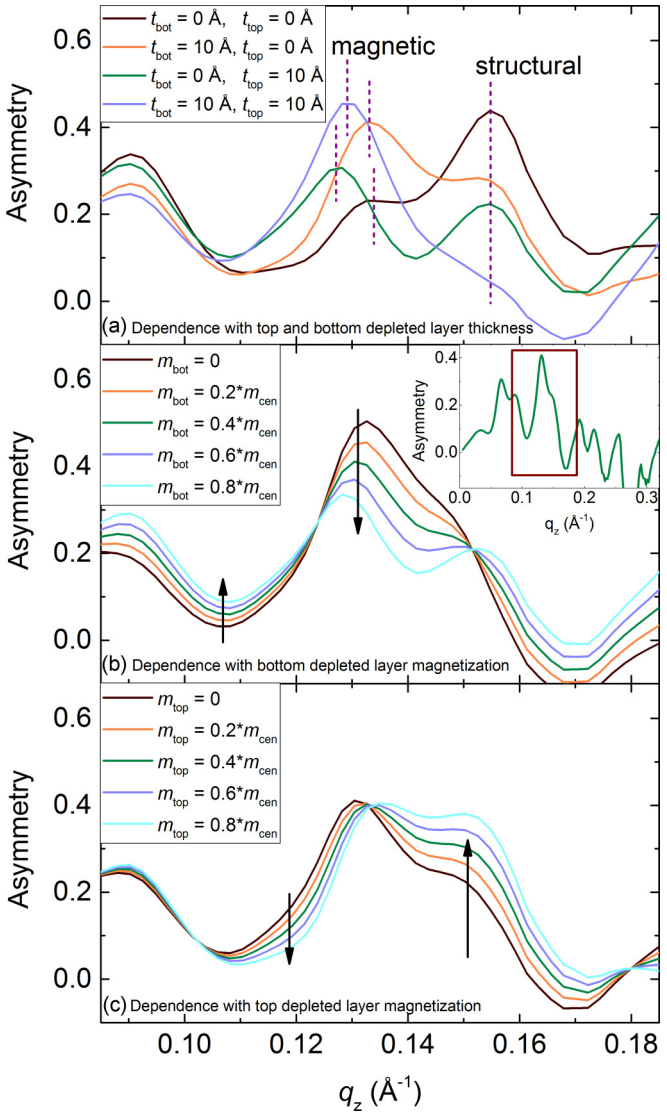

FIG. 6. (Color online) Simulations of the asymmetry ratio at an energy of E_{Mn}, around $q_z = 0.14\,\text{Å}^{-1}$, using a simplistic model of ten repetitions of the same bilayer and zero roughness. (a) The effect of varying the depleted layer thickness. Panels (b) and (c) show the effect of changing the magnetization in the bottom and top depleted layers, respectively. The bottom and top depleted layers were chosen to have thicknesses of 20 and 10 Å, respectively. The inset in (b) shows the asymmetry curve for a wider q_z range.

In Fig. 6 we show the effect of modifying the thicknesses (a) and the magnetization of the top (b) and bottom layers (c). For this demonstration, one of the asymmetry oscillations around $q_z = 0.14\,\text{Å}^{-1}$ was chosen [the full range of which is shown in the inset of Fig. 6(b)].

Figure 6(a) reveals that the double beating at each oscillation of the asymmetry is a signature of the depleted layers. In this example, the total thicknesses of the YBCO and LCMO layers were kept constant, while only the thicknesses of the two depleted layers within them were changed. The result is a two-peaks shape in the asymmetry, the peak on the right, at around $0.15\,\text{Å}^{-1}$ [labeled as "structural" in Fig. 6(a)], which is not very sensitive to the magnetic thickness of the LCMO

TABLE III. Parameter values obtained from the best fits to models YBCO 1.a, YBCO 1.b, and YBCO 2 for the magnetic depth profile of the YBCO layers. t_m is the thickness of the magnetized layers. Separate magnetization values are given for blocks 1 and 2, when applicable (see Fig. 1). In model 2, an interfacial layer due to a BaO plane is considered between the LCMO layer and the magnetic CuO_2 plane. The errors of the magnetization are estimated from the parameter α (see text for more details). The "=" symbol denotes fixed parameters with the same value as in the row above.

	YBCO 1.a ($l_{red} = 0.019$)		YBCO 1.b ($l_{red} = 0.033$)		YBCO 2 ($l_{red} = 0.015$)	
	t_m (± 0.7 Å)	m_{Cu} ($\pm 0.02\,\mu_B$/Cu)	t_m (± 0.7 Å)	m_{Cu} ($\pm 0.02\,\mu_B$/Cu)	t (± 0.7 Å)	m $\pm 0.02\,\mu_B$/Cu)
Block 1	5.4	0.10	5.4	0.11	3.8	0.11
Block 2	4.2	0.28	=	=	=	0.28
BaO planes					2.1	0.0

layer but rather to the periodicity of the magnetization, the effect of the different thickness being reflected in the change of intensities. The peak on the left [labeled as "magnetic" in Fig. 6(a)] is sensitive to the distribution of the magnetization within each LCMO layer, and therefore to the thicknesses of the depleted layer. Figures 6(b) and 6(c) show the effect that variations in m_{top} and m_{bot} have on the asymmetry. In these simulations, we fixed the thicknesses for the top and bottom depleted layers to 10 and 20 Å to emulate the real case of our YBCO/LCMO SL. A redistribution of the asymmetry's intensity was observed [indicated by arrows in Figs. 6(b) and 6(c)]. This redistribution appears to affect regions of each asymmetry oscillation located at lower q_z for the bottom depleted layer (larger distances from the top surface) and regions at larger q_z values for the top depleted layer (smaller distances from the top surface). It is important to note that this intuitive description on the asymmetry, although general, will be highly affected by the roughness of the heterostructure (as is the general case for asymmetry), and thus, an exhaustive study of each particular case would be necessary.

To summarize this section, the high sensitivity of XRMR to small changes in the structure and magnetization allows us to precisely characterize the LCMO magnetic profile. We found that the two interfaces between LCMO and YBCO are not identical, since the depleted layers have different thicknesses and magnetizations. Interestingly, the lower depleted layer has a sizable magnetization whereas the upper depleted layer has a very weak magnetization. These differences between top and bottom LCMO depleted layers might be a result of the PLD growth process. Moreover, the LCMO layers do not change substantially from the bottom to the top of the SL, and only the topmost LCMO layer needs to be accounted for separately.

2. *Cu L_3 absorption edge*

In this section, magnetic depth profiles of YBCO are discussed. The best fits for asymmetry ratios measured at E_{Cu} were obtained for model YBCO 1.a. In this model, we considered two equally thick magnetic layers at the interfaces, characterized by a thickness t_m and a magnetization m_{Cu}. The model used a two-block structure in which the upper YBCO layer is distinguished from the other layers. A sketch of this profile is shown in Fig. 4(h). The best fit for this model is shown in Fig. 4(e), and the resulting values for t_m and m_{Cu} for each block are given in Table III. Models that distinguish between the upper and lower YBCO magnetic layers or include a higher number of blocks were also considered, but despite the increased number of free parameters, the GOF did not considerably improve the fits (similar l_{red}).

In model YBCO 1.b, no distinction is made between different blocks. The best fit to this model is shown in Fig. 4(f), and the corresponding parameters are listed in Table III. In comparison with model YBCO 1.a, model YBCO 1.b falls short in reproducing the fine features of the asymmetry curve. The fine structure, specifically, the three peaks at each oscillation of the asymmetry curve, is better accounted for by introducing a reduced Cu magnetization in the upper YBCO interfacial sublayers, in contrast to the magnetization in the YBCO layers in the remaining part of the SL. The weaker magnetization of the uppermost YBCO layer may be understood as a result of the increased roughness and also the reduced magnetization of the topmost LCMO layer which is in contact with the ambient. As a consequence, the Cu magnetization, measured so far with XMCD in TEY mode, has been underestimated to nearly 30% of the value obtained for the deeper YBCO layers [9].

A possible origin of the Cu magnetic moments is diffusion of Cu atoms into LCMO layers, which may occur during PLD growth. In model 2, we describe the interface using the different atomic planes of YBCO, to show that there is no sign of interdiffusion and that only the Cu moments of the CuO_2 plane closest to the interface contribute to the magnetic signal. For this we divide the YBCO into five sublayers, with stacking sequence BaO-CuO_2-YBCO-CuO_2-BaO (following Ref. [14]); the last CuO chains are missing at the interface with LCMO. The BaO planes were described according to their nominal density and the tabulated scattering amplitudes. The f_m values for Cu around E_{Cu} were used to calculate the scattering amplitudes that correspond to the CuO_2 planes.

The best fit for this model is shown in Table III and Fig. 4(g), and yields a slight improvement of the fitted curve likelihood. The resulting parameters agree with what can be expected from model YBCO 1.a. The magnetization is confined to the CuO_2 planes, and the obtained thicknesses, 3.8 and 2.1 Å, for the CuO and BaO planes, respectively, are close to the nominal values (2.07 Å for the BaO planes and 2.83 Å for the CuO_2 planes). It is important to remark that we can use this model because the interfaces are locally sharp, despite the $\approx$8 Å roughness averaged over the coherence length of the x rays [14].

Finally, we explicitly consider the case of interdiffusion by performing simulations of the two extreme cases in which Cu

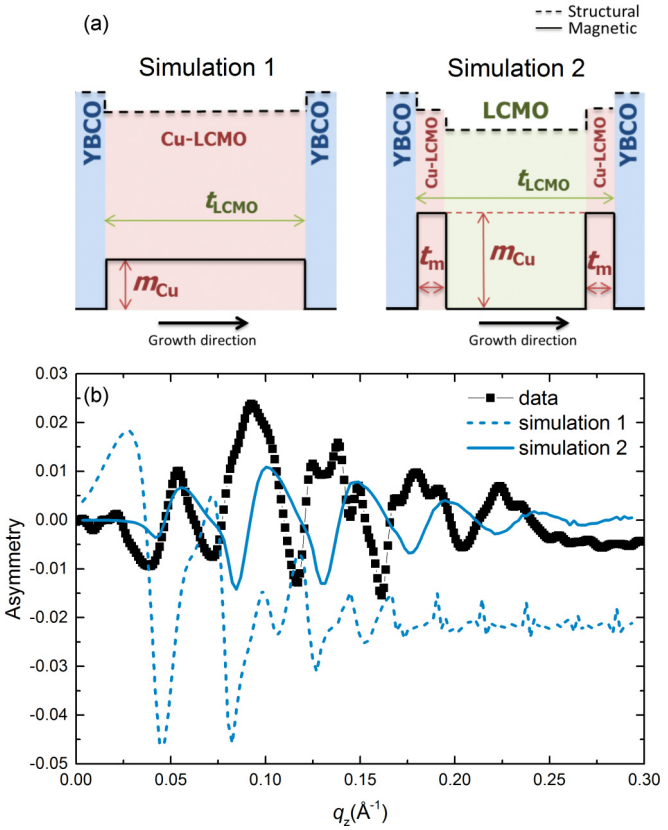

FIG. 7. (Color online) (a) Sketches of the structural (dash lines) and magnetic (solid lines) profiles for each of the two extreme cases of interdiffusion considered: one in which the Cu atoms diffuse across the entire LCMO layer (simulation 1) and another in which the Cu atoms diffuse only to the first 1–2 LCMO unit cells at the interface (simulation 2). (b) Simulations of the asymmetry ratio at the energy E_{Cu} for these two cases.

atoms might diffuse into the LCMO layer. In the first case, Cu atoms diffuse across the whole LCMO layer. In the second case, the diffused Cu atoms remain near the interface, diffusing only over a few unit cells into LCMO. For this purpose, an artificial material in which LCMO is doped with Cu (Cu-LCMO) is defined. This way, the Cu atoms are considered to be homogeneously distributed in the LCMO. The nominal density was calculated and the tabulated values were used to calculate the Cu-LCMO scattering amplitudes. Sketches of these two cases are presented in Fig. 7(a). For the two cases, we calculated the asymmetry for several Cu concentrations. In Fig. 7(b), simulation 1 (dashed line), the first case is shown in which LCMO was substituted by Cu-LCMO (10% Cu-doped) and the LCMO room-temperature value for the thickness was used. Simulation 2 (blue line in Fig. 7) presents the case of a 4-Å-thick Cu-LCMO (also 10% Cu-doped) interfacial layer. We performed this calculation for several thicknesses of the Cu-LCMO interfacial layer, always keeping the total thickness (LCMO + Cu-LCMO) equal to the value obtained at room temperature.

These two simulations demonstrate that in order to reproduce the periodicity of the asymmetry measured using E_{Cu}, the Cu moments must be in the vicinity of the interface, i.e., within a 3–5- Å-thick layer from the interface. For this reason, diffusion of Cu atoms across the entire LCMO layer can be ruled out. For the scenario of short-range diffusion (simulation 2), the periodicity of the asymmetry ratio is nearly recovered, but the maxima and minima of the asymmetry are shifted in their q_z value. This phase change or shift in the asymmetry is a consequence of the structural and magnetic interfaces inside the heterostructure being changed and therefore the interference process modified. However, this shift can be accounted for if the Cu atom direction of the magnetization is assumed to be parallel to the applied magnetic field (i.e., $\gamma = 90°$). But this is in conflict with the XMCD data shown in Fig. 2; short-range diffusion can also be ruled out. In conclusion, by combining the information extracted from the room-temperature and 10-K reflectivity curves, the precise location of the Cu magnetic moments can be deduced and the case of Cu atoms interdiffused in the LCMO can be ruled out.

In summary, in this section we have studied the magnetic depth profile of Cu magnetization in our LCMO/YBCO SL. The magnetic Cu layers are 4.2 Å thick, indicating that the Cu moments are confined to the first interfacial CuO_2 plane. In addition, the resulting magnetization is stronger in deeper YBCO layers (reaching 0.28 μ_B/Cu) but remain similar for the two interfaces, in strong contrast to what is observed in the magnetic profiles of Mn. Interestingly, no differences are found between interfaces in the induced magnetic Cu layer, suggesting that the two manifestations of the MPE in YBCO/LCMO heterostructures (induced Cu magnetization and LCMO depleted layers), despite occurring simultaneously, may be two independent effects. Our models for the Cu asymmetry ratio, which include interdiffusion layers as well as model YBCO 2, confirm that the induced Cu magnetization is not a result of the diffusion of Cu atoms into the LCMO layers but a real proximity effect in which the hybridized Cu atoms obtain a net magnetic moment.

IV. SUMMARY AND CONCLUSIONS

In this paper, we used XRMR to determine the Cu and Mn magnetic depth profiles of a YBCO/LCMO superlattice. This important technique allows probing magnetic interface effects in multilayered systems thanks to its high spacial resolution and sensitivity to small magnetic and structural changes. The YBCO/LCMO heterostructure is formed of two distinct interfaces, differentiated possibly by the growing process: the interfaces in which LCMO is grown on YBCO and the interfaces in which YBCO is grown on LCMO. Here, these two interfaces are found to be not identical due to differences in the so-called LCMO depleted layers. The bottom and top interfaces have a suppressed magnetization, which is nearly complete at the interface in which YBCO is grown on LCMO, whereas a magnetization of 0.62 μ_B per Mn ion is found near the interface where LCMO is grown on YBCO. These differences also concern the thickness of these depleted layers, with the bottom depleted layer being 22 Å and the top depleted layer being 12 Å. Additionally, our study shows that the Cu magnetization does not originate on Cu atoms diffusing into the LCMO but rather a proximity effect in which the magnetization is confined to the CuO_2 plane next to the interface (4.2 Å), with comparable values for the two interfaces.

ACKNOWLEDGMENTS

Experiments were performed at the X11MA and X07MA beamlines at the Swiss Light Source, Paul Scherrer Institut (Villigen, Switzerland). We thank the X11MA and X07MA beamline staff for experimental support. We are grateful to S. Grenier for his help and discussions related to the use of the software DYNA and to D. Satapathy for his participation during the BESSY beamtime. We acknowledge the financial support of Paul Scherrer Institut (PSI) and the Schweizer Natinalfonds (SNF). Y.W.W. is supported through Grant No. 200020-159220 and M.R. through a Sinergia Grant No. 200021-137657. The group at University of Fribourg was supported by the Schweizer Natinalfonds (SNF) through Grants No. 200020-153660 and No. CRSII2-154410/1.

[1] H. Y. Hwang, Y. Iwasa, M. Kawasaki, B. Keimer, N. Nagaosa, and Y. Tokura, Nature Mater. **11**, 103 (2012).

[2] J. Chakhalian, J. W. Freeland, C. Panagopoulos, and J. M. Rondinelli, Rev. Mod. Phys. **86**, 1189 (2014).

[3] E. Dagotto, Science **309**, 257 (2005).

[4] A. Ohtomo and H. Y. Hwang, Nature **427**, 423 (2004).

[5] E. Benckiser, M. W. Haverkort, S. Bruck, E. Goering, S. Macke, A. Fraño, X. Yang, O. K. Andersen, G. Cristiani, H.-U. Habermeier, A. V. Boris, I. Zegkinoglou, P. Wochner, H.-J. Kim, V. Hinkov, and B. Keimer, Nature Mater. **10**, 189 (2011).

[6] M. Gibert, P. Zubko, R. Scherwitzl, J. Iñiguez, and J.-M. Triscone, Nature Mater. **11**, 195 (2012).

[7] J. Stahn, J. Chakhalian, C. Niedermayer, J. Hoppler, T. Gutberlet, J. Voigt, F. Treubel, H.-U. Habermeier, G. Cristiani, B. Keimer, and C. Bernhard, Phys. Rev. B **71**, 140509 (2005).

[8] J. Chakhalian, J. W. Freeland, G. Srajer, J. Strempfer, G. Khaliullin, J. C. Cezar, T. Charlton, R. Dalgliesh, C. Bernhard, G. Cristiani, H.-U. Habermeier, and B. Keimer, Nat. Phys. **2**, 244 (2006).

[9] D. K. Satapathy, M. A. Uribe-Laverde, I. Marozau, V. K. Malik, S. Das, Th. Wagner, C. Marcelot, J. Stahn, S. Bruck, A. Ruhm, S. Macke, T. Tietze, E. Goering, A. Frano, J.-H. Kim, M. Wu, E. Benckiser, B. Keimer, A. Devishvili, B. P. Toperverg, M. Merz, P. Nagel, S. Schuppler, and C. Bernhard, Phys. Rev. Lett. **108**, 197201 (2012).

[10] M. A. Uribe-Laverde, D. K. Satapathy, I. Marozau, V. K. Malik, S. Das, K. Sen, J. Stahn, A. Ruhm, J.-H. Kim, T. Keller, A. Devishvili, B. P. Toperverg, and C. Bernhard, Phys. Rev. B **87**, 115105 (2013).

[11] C. F. Majkrzak, K. V. O'Donovan, and N. F. Berk, Physica B **173**, 75 (1991).

[12] Z. Sefrioui, D. Arias, V. Pena, J. E. Villegas, M. Varela, P. Prieto, C. Leon, J. L. Martinez, and J. Santamaria, Phys. Rev. B **67**, 214511 (2003).

[13] V. Pena, Z. Sefrioui, D. Arias, C. Leon, J. Santamaria, M. Varela, S. J. Pennycook, and J. L. Martinez, Phys. Rev. B **69**, 224502 (2004).

[14] V. K. Malik, I. Marozau, S. Das, B. Doggett, D. K. Satapathy, M. A. Uribe-Laverde, N. Biskup, M. Varela, C. W. Schneider, C. Marcelot, J. Stahn, and C. Bernhard, Phys. Rev. B **85**, 054514 (2012).

[15] J. Chakhalian, J. W. Freeland, H.-U. Habermeier, G. Cristiani, G. Khaliullin, M. van Veenendaal, and B. Keimer, Science **318**, 1114 (2007).

[16] M. A. Uribe-Laverde, S. Das, K. Sen, I. Marozau, E. Perret, A. Alberca, J. Heidler, C. Piamonteze, M. Merz, P. Nagel, S. Schuppler, D. Munzar, and C. Bernhard, Phys. Rev. B **90**, 205135 (2014).

[17] S. Bruck, S. Treiber, S. Macket, P. Audehm, G. Christiani, S. Soltan, H-U. Habermeier, E. Goering, and J. Albrecht, New J. Phys **13**, 033023 (2011).

[18] U. Staub, V. Scagnoli, Y. Bodenthin, M. Garca-Fernandez, R. Wetter, A. M. Mulders, H. Grimmer, and M. Horisberger, J. Synchrotron Radiat. **15**, 469 (2008).

[19] U. Flechsig, F. Nolting, A. Fraile Rodriguez, J. Krempasky, C. Quitmann, T. Schmidt, S. Spielmann, and D. Zimoch, AIP Conf. Proc. **1234**, 319 (2010).

[20] C. Piamonteze, U. Flechsig, S. Rusponi, J. Dreiser, J. Heidler, M. Schmidt, R. Wetter, M. Calvi, T. Schmidt, H. Pruchova, J. Krempasky, C. Quitmann, H. Brune, and F. Nolting, J. Synchrotron Radiat. **19**, 661 (2012).

[21] S. Bruck, S. Bauknecht, B. Ludescher, E. Goering, and G. Schutz, Rev. Sci. Instrum. **79**, 083109 (2008).

[22] M. Elzo, E. Jal, O. Bunau, S. Grenier, Y. Joly, A. Y. Ramos, H. C. N. Tolentino, J. M. Tonnerre, and N. Jaouen, J. Magn. Magn. Mater. **324**, 105 (2012).

[23] L. G. Parratt, Phys. Rev. **95**, 359 (1954).

[24] S. A. Stepanov and S. K. Sinha, Phys. Rev. B **61**, 15302 (2000).

[25] J. P. Hannon, G. T. Trammell, M. Blume, and Doon Gibbs, Phys. Rev. Lett **61**, 1245 (1988).

[26] J. P. Hill and D. F. McMorrow, Acta Cryst. **A52**, 236 (1996).

[27] J. B. Kortright and Sang-Koog Kim, Phys. Rev. B **62**, 12216 (2000).

[28] C. T. Chantler, J. Phys. Chem. Ref. Data **29**, 597 (2000).

[29] J. J. Hoyt, D. de Fontaine, and W. K. Warburton, J. Appl. Cryst. **17**, 344 (1984).

[30] E. Jal, M. Dąbrowski, J. M. Tonnerre, M. Przybylski, S. Grenier, N. Jaouen, and J. Kirschner, Phys. Rev. B **91**, 214418 (2015).

[31] J. M. Tonnerre, N. Jaouen, E. Bontempi, D. Carbone, D. Babonneau, M. de Santis, H. C. N. Tolentino, S. Grenier, S. Garaudee, and U. Staub, J. Phys. Conf. Series **211**, 012015 (2010).